

G.L. Falchetto, D. Coster, R. Coelho, B.D. Scott, L. Figini, D. Kalupin, L.L. Alves, V. Basiuk, João P.S. Bizarro, C. Boulbe, A. Dinklage, D. Farina, B. Faugeras, J. Ferreira, A. Figueiredo, Ph. Huynh, F. Imbeaux, I. Ivanova-Stanik, T. Jonsson, H-J. Klingshirn, C. Konz, A. Kus, N.B. Marushchenko, E. Nardon, S. Nowak, G. Pereverzev, M. Owsiak, E. Poli, Y. Peysson, R. Reimer, J. Signoret, O. Sauter, R. Stankiewicz, P. Strand, I. Voitsekhovitch, E. Westerhof, T. Zok, W. Zwingmann, ITM-TF contributors, the ASDEX Upgrade Team and JET-EFDA Contributors

The European Integrated Tokamak Modelling (ITM) Effort: Achievements and First Physics Results

“This document is intended for publication in the open literature. It is made available on the understanding that it may not be further circulated and extracts or references may not be published prior to publication of the original when applicable, or without the consent of the Publications Officer, EFDA, Culham Science Centre, Abingdon, Oxon, OX14 3DB, UK.”

“Enquiries about Copyright and reproduction should be addressed to the Publications Officer, EFDA, Culham Science Centre, Abingdon, Oxon, OX14 3DB, UK.”

The contents of this preprint and all other JET EFDA Preprints and Conference Papers are available to view online free at www.iop.org/Jet. This site has full search facilities and e-mail alert options. The diagrams contained within the PDFs on this site are hyperlinked from the year 1996 onwards.

The European Integrated Tokamak Modelling (ITM) Effort: Achievements and First Physics Results

G.L. Falchetto¹, D. Coster², R. Coelho³, B.D. Scott², L. Figini⁴, D. Kalupin⁵,
L.L. Alves³, V. Basiuk¹, João P.S. Bizarro³, C. Boulbe⁶, A. Dinklage⁷, D. Farina⁴, B. Faugeras⁶,
J. Ferreira³, A. Figueiredo³, Ph. Huynh¹, F. Imbeaux¹, I. Ivanova-Stanik⁸, T. Jonsson⁹,
H-J. Klingshirn², C. Konz², A. Kus⁷, N.B. Marushchenko⁷, E. Nardon¹, S. Nowak⁴,
G. Pereverzev[‡], M. Owsiak¹⁰, E. Poli², Y. Peysson¹, R. Reimer⁷, J. Signoret¹, O. Sauter¹¹,
R. Stankiewicz⁸, P. Strand¹², I. Voitsekhovitch¹³, E. Westerhof¹⁴, T. Zok¹⁰, W. Zwingmann¹⁵,
ITM-TF contributors[†], the ASDEX Upgrade Team^{††} and JET-EFDA Contributors*

JET-EFDA, Culham Science Centre, OX14 3DB, Abingdon, UK

¹*CEA, IRFM, F-13108 Saint-Paul-lez-Durance, France.*

²*Max-Planck-Institut für Plasmaphysik, EURATOM-IPP Association, Garching, Germany*

³*Associação EURATOM/IST, Instituto de Plasmas e Fusão Nuclear, Instituto Superior Técnico,
Universidade Técnica de Lisboa 1049-001 Lisboa, Portugal*

⁴*Istituto di Fisica del Plasma CNR, Euratom-ENEA-CNR Association, 20125 Milano, Italy*

⁵*EFDA-CSU Garching, Boltzmannstr. 2, D-85748, Garching, Germany*

⁶*University Nice Sophia Antipolis, Laboratory JA Dieudonne, UMR 7351, F-06108 Nice 02, France*

⁷*Max Planck Institut für Plasmaphysik, EURATOM Association, Greifswald, Germany*

⁸*Institute of Plasma Physics and Laser Microfusion, EURATOM Association, 00-908 Warsaw, Poland*

⁹*Association EURATOM-VR, Fusion Plasma Physics, EES, KTH, SE-10037 Stockholm, Sweden*

¹⁰*Poznan Supercomputing and Networking Center, IChB PAS, Noskowskiego 12/14, Poznan, Poland*

¹¹*Ecole Polytechnique Federale de Lausanne (EPFL), Centre de Recherches en Physique des Plasmas (CRPP),
Association Euratom-Confederation Suisse, Lausanne, Switzerland*

¹²*Department of Earth and Space Sciences, Chalmers University of Technology,
EURATOM-VR Association, SE-352 96 Göteborg, Sweden*

¹³*EURATOM-CCFE Fusion Association, Culham Science Centre, OX14 3DB, Abingdon, OXON, UK*

¹⁴*FOM Institute DIFFER, Association EURATOM-FOM, Nieuwegein, Netherlands*

¹⁵*European Commission, Directorate-General for Research and Innovation, B-1049 Brussels, Belgium*

* See annex of F. Romanelli et al, "Overview of JET Results",
(24th IAEA Fusion Energy Conference, San Diego, USA (2012)).

Preprint of Paper to be submitted for publication in
Nuclear Fusion

ABSTRACT.

A selection of achievements and first physics results are presented of the European Integrated Tokamak Modelling Task Force (EFDA ITM-TF) simulation framework, which aims to provide a standardized platform and an integrated modelling suite of validated numerical codes for the simulation and prediction of a complete plasma discharge of an arbitrary tokamak. The framework developed by the ITM-TF, based on a generic data structure including both simulated and experimental data, allows for the development of sophisticated integrated simulations (workflows) for physics application. The equilibrium reconstruction and linear MHD stability simulation chain was applied, in particular, to the analysis of the edge MHD stability of ASDEX Upgrade type-I ELMy H-mode discharges and ITER hybrid scenario, demonstrating the stabilizing effect of an increased Shafranov shift on edge modes. Interpretive simulations of a JET hybrid discharge were performed with two electromagnetic turbulence codes within ITM infrastructure showing the signature of trapped-electron assisted ITG turbulence. A successful benchmark among five EC beam/ray-tracing codes was performed in the ITM framework for an ITER inductive scenario for different launching conditions from the Equatorial and Upper Launcher, showing good agreement of the computed absorbed power and driven current. Selected achievements and scientific workflow applications targeting key modelling topics and physics problems are also presented, showing the current status of the ITM-TF modelling suite.

1. INTRODUCTION

The European Integrated Tokamak Modelling Task Force (ITM-TF) [1,2] aims at providing a standardized platform and an integrated modelling suite of validated numerical codes for the simulation and prediction of a complete plasma discharge in arbitrary tokamaks. In order to address such a challenge, the ITM-TF approach builds on a modelling infrastructure, focusing on the development of a data and communication ontology, i.e., standardizing the data exchange between different codes, through a generic data structure incorporating both simulated and experimental data. The elements of this data structure are identified as “Consistent Physical Objects”, or CPO [3]. Physics modules of various complexities can be easily adapted to the data structure, which is code and language agnostic, and thus coupled and interchanged in an integrated simulation (workflow). The physics modules integrated into ITM workflows are being cross-verified within the ITM framework as well as against existing integrated modelling codes to guarantee both their interchangeability and their validation. Moreover, in the ITM-TF framework all machine related data are extracted into standardized machine descriptions (MD) so that physics modules, like equilibrium reconstruction tools, also become independent of the specific tokamak experiment. The ITM-TF uses the open-source Kepler[†] scientific workflow manager and orchestrator tool, which allows for a user-friendly graphical construction of the integrated simulation. Physics modules enter as *actors* of a Kepler workflow. It has to be noted, though, that the generic datastructure is totally independent of the used workflow orchestrator tool - all the advantages of the generic datastructure remain if the physics

[†]<http://kepler-project.org>

modules are called in a classic Fortran workflow, with CPOs as arguments.

The framework developed by the ITM-TF has allowed for the development of sophisticated workflows for physics applications. Those include the European Transport Simulator (ETS) [4], a leading ITM tool for both interpretive and predictive transport simulations and scenario modelling, incorporating a sophisticated module for synergy effects between heating schemes, several equilibrium modules, pellets, impurities, neutrals, sawteeth and neoclassical tearing modes (NTM) modules, as well as a variety of neoclassical and turbulence transport modules of different complexity.

In this paper, selected achievements targeting key modelling topics and physics problems are outlined, showing the present status of the ITM-TF modelling suite. Physics results on the MHD equilibrium and linear stability of the plasma edge of ASDEX Upgrade and ITER hybrid scenario [5] as well as interpretive studies of a JET discharge using gyrofluid and gyrokinetic turbulence models are reported in Section 2. Results from a thorough benchmarking of electron cyclotron heating and current drive codes [6] on an ITER H-mode scenario for different launching conditions both from the Equatorial Launcher (EL) and Upper Launcher (UL) are shown in Section 3.1 Section 3.2 reports the ETS successful benchmarking against leading tokamak plasma core transport codes on a JET hybrid discharge [7]. In order to illustrate the flexibility and wide range of use cases for scientific workflows, Section 4 focuses on some relevant examples. Firstly, application of a direct coupling of the ETS core transport solver to a 2D edge transport code, demonstrated for the particular case of steady state and multiple impurities [8], is shown. The second example addresses the effect of NTMs on plasma transport and confinement, incorporated in ETS workflows via a dedicated NTM module that calculates the island frequency, width and associated reshaping in transport coefficients. Lastly, a successful proof-of-principle application of an ETS workflow including the coupling with a free-boundary equilibrium code, to the simulation of a VDE, is presented. In Section 5 recent results are shown of the ongoing effort in ITM-TF to incorporate synthetic diagnostics [9] into the modelling framework (fusion products, 3D reflectometry, Motional Stark Effect, neutron and Neutral Particle Analyser), focusing on synthetic Motional Stark Effect spectra and comparison to the experimental data.

2. PHYSICS RESULTS

A selection of some of the first physics results produced using the ITM-TF framework is presented in the following subsections.

2.1 EQUILIBRIUM RECONSTRUCTION AND LINEAR MHD STABILITY

The first demonstration of the use of ITM-TF integrated simulation workflows for physics studies on experimental data addressed equilibrium reconstruction, refinement and linear MHD stability calculations [5]. The corresponding Kepler workflow is illustrated in Figure 1, *actors* for free-boundary equilibrium reconstruction (e.g. EQUAL[10,11]), high resolution fixed-boundary Grad-

Shafranov solver (e.g. HELENA [12] or CHEASE [13]), and linear MHD stability (e.g. ILSA[14] or MARS-F [15]) are seamlessly integrated in the workflow environment. The machine independent equilibrium reconstruction code EQUAL developed within the ITM-TF has been extensively validated (at a first stage with magnetic data only) on JET discharges [16].

An analysis of the edge MHD stability of ASDEX Upgrade type-I ELMy H-mode discharges was carried out, using the stability chain coupling CLISTE, HELENA and ILSA (used in MISHKA operation mode [13])[5]. Replacing the equilibrium actor with a JALPHA actor, which reads a previously calculated fixed boundary equilibrium from the database, modifies the pressure profile and/or the flux surface averaged current density and computes the new high resolution equilibrium, a j - α workflow is created. Stability diagrams can then be automatically computed using Kepler, by wrapping the linear j - α workflow in a double loop over the pressure and current scaling parameters. Computation times being substantial for such scans, the ITM-TF developed, in cooperation with the FP7 project EUFORIA [17], Kepler workflows for automatic job submission to Grid and Cloud infrastructures.

For pedestal height studies, the pressure and current density profiles in the edge can be scaled by a constant factor, while the core profiles are adapted to keep the plasma energy W_{MHD} and the total plasma current I_p unchanged. For pedestal width studies, the widths of the pressure and current density pedestals can be scaled independently, again adjusting the core profiles such that W_{MHD} and I_p remain the same. In this case, the pressure at the pedestal top and the amplitude of the bootstrap current remain constant, only the gradients change through variation of the width. Therefore, the total current flowing in the edge is smaller if the width is reduced.

Figure 2 shows the stability diagrams for the variation of the pedestal height and width for ASDEX Upgrade Pulse No: 23223 at $t = 5.33\text{s}$. The profiles were taken just before the crash of type-I ELMs. As expected, the experimental equilibrium is marginally unstable with a toroidal mode number ($n = 5$) indicating a strong peeling component. Reducing the pedestal width, and thereby increasing the gradients, clearly drives the equilibrium unstable. It may also be noted that the drive from the current density gradient (small bootstrap current width) dominates the drive from larger edge current (large bootstrap current width).

Core and pedestal scans of the normalized plasma beta β_N were also performed using the linear MHD stability chain for the ASDEX Upgrade type-I ELMy Pulse No: 20116 at $t = 3.59\text{s}$ as well as an ITER hybrid scenario (Figure 3). It is evident from the computed growth rates in dashed lines that the increased Shafranov shift helps stabilizing edge modes. When scaling the entire pressure profile (solid lines), the destabilizing effect of the larger edge pressure gradient strongly dominates over the stabilizing effect by the Shafranov shift.

2.2. TURBULENCE SIMULATIONS

A simple workflow allows conventional methods of comparing a turbulence code's transport results to experimental measurements and transport analysis. Run in a double-blind fashion, the result is

almost always discrepant. Physical insight into the problem usually depends on diagnosing these discrepancies. An hybrid JET Pulse No: (77922) was used as a very interesting test-bed for radially local turbulence/transport computations, which happen to fail due to the set of parameters in the core-confinement region (between 0.4 and 0.7 in normalized radius).

Discussions on the observed discrepancies among different turbulence/transport code simulations highlighted several issues of provenance, namely what is used for the equilibrium flux surface structure, and what is used to define the dimensionless parameters of the runs (in this case, gradients). The profiles of the case under study turned out to be close enough to stability thresholds that small differences in magnetic shear or in the choice of radial coordinates (eg, ρ_{tor} versus the midplane-cut minor radius) are enough to make the difference between stability and weak turbulence.

The prescribed case was profile data from JET Pulse No: 77922 at time 47.7sec. The input data were provided by TRANSP in interpretive mode from the actual experimental data which determine the profiles. Profiles of the electron density, electron and ion temperatures (ions hotter), and the toroidal current and pitch parameter q are shown in Figure 4.

The case is read from the database into coreprof and equilibrium CPOs, and then fed to the rest of the workflow, represented in Figure 5. Since the equilibrium CPO did not contain sufficient information as needed by the successive flux-tube turbulence code modules (namely the pressure profile and the straight-field-line coordinate metric were missing), the workflow consisted of three actors: EQUUPDATE which constructs equilibrium profile inputs for pressure and toroidal current from coreprof_CPO, and passes the equilibrium boundary surface, in this case the experimental separatrix, then the fixed-boundary Grad-Shafranov solver GKMHD which also fills the coord_sys element in the equilibrium_CPO, and then the turbulence code GEM, a fluxtube gyrofluid model [18]. GEM actor is executed in batch on HPC-FF, running in parallel one fluxtube at each of 0.4, 0.5, 0.6, and 0.7 normalised midplane-cut minor radius, it fills the coretransp_CPO and also provides the standard post-process diagnostics for turbulence.

The delta-FEFI turbulence code, a delta-f gyrokinetic parent model to GEM otherwise similar in structure [19]), was also run replacing GEM in the same workflow, obtaining useful results at the 0.6 normalised radius for direct comparisons between the two models.

The use of the GKMHD module was needed because a theoretical s - α model was found to be a very poor approximate to these experimental cases which are in the shaped geometry of a diverted tokamak. GKMHD sets up a regular triangular grid logically the same as placing flux surfaces onto nested hexagons. Each iteration consists of solving $-\mu_0 \Delta^* \psi = \langle J_{\text{tor}} R \rangle + \mu_0 (dp/d\psi)(R^2 - \langle R^2 \rangle)$ where $\langle \rangle$ denotes flux surface average, p and $\langle J_{\text{tor}} R \rangle / R_0$ are the input profiles, and then moving the grid points towards or away from the axis such that the prescribed normalised ψ of the surface agrees with the new values of $\psi(R,Z)$. Otherwise it is a conventional Grad-Shafranov solver taking pressure and current on input. Afterwards, the resulting equilibrium CPO is filled with coordinate metric information needed by fluxtube models. The midplane-cut minor radius is defined as $(r_{\text{outboard}} - r_{\text{inboard}})/2$ from the equilibrium CPO; the normalised version is denoted as r_a below. Both GEM

and delta-FEFI take the straight-field-line coordinate metric on input and construct a field-aligned, shifted-metric coordinate system based on Hamada coordinates[20][21]. The fluctuations are initialised as a single Maxwellian density structure localised at nonlinear amplitude with Gaussian profiles to 10 ion sound gyroradii (ρ_s) in the drift plane and to qR_0 along the field lines. The finite electron pressure launches shear-Alfvén waves and then a drift wave field at nonlinear amplitude, and the system proceeds to fully developed turbulence unless it is nonlinearly stable [20][23].

Gyrofluid runs are held in saturation or decay for 4000 gyro-Bohm times ($\tau_{GB} = L_{\perp}/c_s$, where L_{\perp} is the steepest gradient scale length, usually that of T_e but not always [22]). Gyrokinetic runs only went to $1000 L_{\perp}/c_s$ due to the far greater computational expense. Since conditions can generally be either edge or core, the computational setup must be compatible with either. We therefore set up for core rules which are more difficult [24]. Each fluxtube is an independent run, with its own normalised units including normalised time, τ_{GB} being different for each case. The timestep is $0.002\tau_{GB}$, allowing for extreme transients which are found in the early stages of some core-parameter cases. The domain size is $20\pi\rho_s$ in the radial direction, $80\pi\rho_s$ in the drift-angle direction, and one connection length $2\pi qR$ in the parallel direction. The grid is $128 \times 128 \times 32$ in these directions, respectively. The 4×1 rules for both domain size aspect ratio and radial/drift-angle resolution are of central importance to account for the properties of this type of turbulence [24]. The setup of the field alignment and parallel field-line connection is given in [21]. The radial boundary conditions are Dirichlet; a good description of how to treat them is given in [23]. The numerical scheme is given in [18], mostly following [23]. Delta-FEFI uses the same scheme as GEM with the additional ingredient being the phase-space parallel bracket [19].

We concentrate on the case $r_a = 0.6$ since both codes found stability or on-threshold behaviour at 0.7 ; delta-FEFI crashed at 0.4 and 0.5 apparently due to difficulty with the kinetic ballooning mode, KBM (the code has never managed a saturated nonlinear-KBM case). Interestingly, GEM did not find any KBM but stability at 0.4 , a very weak ITG case at 0.5 , a weak-to-stable ITG case at 0.6 , with ion heat flux < 0.1 in gyro-Bohm units of $p_e c_s (\rho_s / L_{\perp})^2$, and approximately null growth, not obviously damped or growing, at 0.7 . The above are identified not by linear mode properties but by energetics: ITG cases have dominantly ExB/ion-gradient energetics, microtearing has magnetic-flutter/electron-gradient energetics [22] and KBM has a combination of ExB pressure-gradient and magnetic-flutter/electron-gradient energetics, with the electron magnetic flutter transport becoming positive and equally large as the ExB transport. In all these cases the density gradient is subdominant and although particle fluxes are positive the energetics is very weak compared to the temperature gradients. ITG mode structure is characterised by fluctuations in the perpendicular ion temperature having the largest relative amplitude and strongest ballooning factors (at least twice as large as $e \Phi_{fl}/T_e$). For edge cases the electron grad-T drive can be comparable despite the smaller fluctuation level but for core cases the grad- T_e drive is smaller by a factor between 5 and 10 .

The delta-FEFI results were quite different. Besides the two KBM crashes at $r_a = 0.4$ and 0.5 , the $r_a = 0.7$ case was definitively stable and the $r_a = 0.6$ case produced what can be identified as a

strongly trapped-electron enhanced ITG case which is worth showing. The normalised parameters are [24] $\beta\text{-hat} = 0.38$, $\mu\text{-hat} = 0.022$, $C = 3 \times 10^{-4}$, $T_i/T_e = 1.25$, $R/L_{Ti} = 6.30$, $L_{Ti}/L_{Te} = 0.68$, $L_{Ti}/L_n = 0.38$, and $qR_0/L_{Ti} = 9.0$.

The transport, shown in Figure 6 is bursty following the quasi-periodic appearance and destruction by turbulence of radial streamers. The ion heat flux is well over 1 in gyro-Bohm units during the bursts, and the average is about 0.81 in the $400 < t/\tau_{GB} < 1000$ interval. The electron heat flux is about 0.29; these numbers are more than one order of magnitude larger than the GEM values at $r_a = 0.5$ and 0.6. The energetics (not shown) indicates an ion drive about 10 times larger than the electron one (T_i is about 1.4 times steeper and the ions are hotter). The response to the density blob yields a spectrum peak at $k_{\perp}\rho_s \sim 0.2$, with a negligible subsequent spectral shift. The peak (Figure 7) is not as narrow in saturation as during the streamer phases. All of the fluctuation amplitude spectra have the same shape; there is no flattening of the vorticity and current spectra as seen in edge turbulence.

The parallel fluctuation envelopes (squared amplitudes or transport fluxes integrated over the perpendicular plane, expressed as functions of the parallel coordinate s [26]), shown in Figure 8, are not unusual, $T_{i\parallel}$ is slightly larger than $e\Phi/T_e$ and equally two-to-one ballooned, but $T_{i\perp}$ is about three times larger and more like four-to-one ballooned. This is a hallmark of ITG signature. In the flux surface averages (not shown), no significant zonal flow activity is observed (this tends to be weakened by the finite β for core cases [26]). The contours (Figure 9) show the obvious streamers ($\lambda_x/\lambda_y > 2$ in the correlation lengths) in the density fluctuations, with the streamer break caused by nonlinear shifts in the fluctuation shape followed by destruction of the streamers. The motion of the structures at the beginning of the break (out for positive, in for negative) is a clear indication of the convective $\delta\text{-}f \text{ ExB}$ nonlinearity as the same effect is seen in edge turbulence at the transition to nonlinearity from a linear start [25].

In the gyrofluid case the degree of small-scale radial hash on the structures is more visible, since every degree of freedom is subject to field line connection, while here in the gyrokinetic case the large influence of trapped electrons in the overall dynamics produces much smoother contour structure

The most interesting finding, however, is in the velocity space distribution of the contributions of $\delta\text{-}f$ to the turbulent ExB fluxes, shown in Figure 10. All of the activity in the electrons and almost all in the ions is in the trapped domain (smaller v -parallel for finite μB). This is the clearest-possible identifier for a role of trapped electrons despite the ion-dominant energetics and is the basis for the named *trapped-electron assisted ITG turbulence*. That this is indeed turbulence- and not a set of coherent modes- is indicated by the fluctuation statistics, amplitude PDFs of electrostatic potential and ion temperature fluctuations and phase shift distributions in the electron density and electrostatic potential fluctuations, shown in Figure 11. These are classic drift-wave turbulence signatures [26].

3. VERIFICATION AND VALIDATION

The ITM-TF framework is a valuable environment for a rigorous cross-verification of codes describing the same physics processes with different models, since by interchanging those as modules within the same workflow the possible external sources of discrepancy are minimized. Considering the fundamentals of an integrated transport simulator, it is essential to address the benchmarking of the equilibrium and core profile evolution solvers as well as the transport and turbulence or heating and current drive modules. Equilibrium codes went through benchmarking both within the ETS workflow [27] and independently, whereas turbulence and MHD codes cross-verification is ongoing on specified test cases within dedicated workflows. In this section the benchmarking of standalone electron cyclotron heating and current drive codes on an ITER scenario as well as the ETS validation against existing integrated modelling transport codes on a JET hybrid discharge are presented. It has to be mentioned that the ETS was previously extensively verified [28][6]. The very good agreement achieved for the simulated quantities and applied modules lays the foundations for the use of ETS for both predictive and interpretative runs on present devices and ITER, in a variety of scenarios.

3.1 BENCHMARKING OF ELECTRON CYCLOTRON HEATING AND CURRENT DRIVE CODES ON AN ITER SCENARIO

A benchmark among five European EC beam/ray-tracing codes (C3PO [29], GRAY [30], TORAY-FOM [31], TORBEAM [32], TRAVIS[33]) has been successfully performed [6] within the ITM framework for a standard inductive H-mode ITER scenario (“Scenario 2”) for three different launching conditions both from the Equatorial Launcher (EL) and Upper Launcher (UL), see Table I. The three cases have been selected to cover different geometries and physics: divergent beam absorbed in the core (EL25), interaction dominated by Doppler broadening (EL40), focused beam (UL). The frequency of the launched beam is 170 GHz and the input power is 1 MW.

The steps taken in the benchmarking study consisted in: (i) an extensive check of matching between ITM’s and all codes’ coordinate and sign conventions as well as physical quantities definitions, to ensure that the input and output data were correctly interpreted and written by the codes; (ii) a comparison among the computed wave trajectories, with particular consideration of the vacuum-plasma transition; (iii) a comparison of the power absorption and current drive results. Good agreement was found, with differences in total current $|\delta I_{CD}/I_{CD}| < 15\%$, and with peak values of power density dP/dV and driven current density typically matching within 10%, and the position of the profiles match within $\delta\rho \sim 0.02$ in normalized radius units (Figure 12). Small discrepancies can be ascribed to the different models used for wave propagation and absorption and current drive. In the EL40 case Doppler broadening dominates the effect of finite beam size in the determination of the profiles width, and all the codes here agree very well. In the UL case, despite the focused beam, the profiles are reasonably well reconstructed also by ray-tracing codes, giving results comparable to those obtained by the codes which account for diffraction effects. The large edge density gradient,

and long path from boundary to absorption region, amplifies the impact of edge refraction on beam propagation. However, the influence of the observed discrepancies on computed power and current density profiles is still moderate. Only in case of strongly focused beam, like in the UL case, the uncertainty may approach the profiles width. Deeper analysis of the discrepancies among the different codes and underlying models used for wave propagation, absorption and current drive is ongoing and will be presented in a following publication [33].

3.2 EUROPEAN TRANSPORT SOLVER VALIDATION

A rigorous benchmarking of the ETS against ASTRA[35] and CRONOS[36] integrated modelling transport codes was performed by using the parameters of JET hybrid Pulse No:77922 with current overshoot, $B_{\text{tor}} = 2.3$ T, $I_{\text{pl}} = 1.7$ MA, high triangularity (0.38), 18MW of NBI, $n_1 = 4.8 \cdot 10^{19} \text{ m}^{-3}$, $\beta_N = 2.8$. Self-consistent evolution of electron and ion temperatures, current diffusion and equilibrium (the three moments equilibrium module EMEQ[35] was used both within the ETS and ASTRA, whereas HELENA[12] was used within CRONOS) was simulated. Spitzer resistivity was used for the current transport and the heat transport coefficients were provided by a Bohm - gyroBohm transport model. The simulations were performed with a fixed electron density profile measured at 7.7 s of shot #77922. Gaussian heating and current drive profiles (centred at $\rho = 0$, half-width $\Delta\rho = 0.3$), with a total heating power $P_{\text{tot}} = 18\text{MW}$, distributed 70/30 between ions and electrons, were used in all codes. A beam-driven current $I_{\text{ni}} = 0.12\text{MA}$ was imposed in all simulations while the bootstrap current was neglected. With these assumptions, the simulations were performed for 40 s reaching a steady state solution.

A satisfactory agreement was obtained on the temperatures and q-profile simulated by the three codes as well as on the computed thermal diffusivities (Figure 13) [7]. The slight differences in profiles can be attributed to the different equilibrium solvers used within the compared codes.

4. ITM-TF WORKFLOW APPLICATIONS

4.1 CORE-EDGE COUPLING

Coupling codes, besides the complexity of dealing with separate codes eventually presenting mixed-language programming, which is indeed overcome by the ITM-TF approach, introduces a number of issues to be dealt with: disparity in time-scales, different physics assumptions and scheduling the interaction between the coupled codes.

The core-edge coupled system does introduce a disparity in time-scales, with a characteristic time-scale for the core being an energy confinement time or longer (seconds), whereas the Scrape-Off Layer (SOL) typically has a time-scale of milliseconds with some phenomena being even faster. Another disparity is the computational complexity: transport solvers for the core are typically 1D (radial) codes solving a set of reaction-convection-diffusion equations evolving the density, toroidal momentum and energies for the species considered; edge transport solvers are typically a 2D (radial and poloidal with toroidal symmetry assumed) or 3D code solving for the density, parallel

momentum and energies for the species considered and are thus considerably more expensive computationally. Moreover impurities in the core are often split off from the main ion species and only the density equations are solved for the various impurity charge states. The coupling effort is significantly simplified in the case one is interested in finding a consistent steady state solution between the core and edge codes, which is the problem addressed here.

Three approaches for core-edge coupling can be used, as described in [37]: *mediated*, where the edge codes are used to provide boundary conditions for the core codes on the basis of fitting coefficients to the results of a number of edge runs; *direct* where the edge and core codes are directly coupled; and *avoided* where the edge code is extended all the way to the centre of the plasma. Here we present the direct coupling of an edge and a core transport code via a Fortran workflow using the ITM-TF infrastructure (ie CPOs) for the particular case of steady state and multiple impurities [8].

The edge 2D transport code (SOLPS) [38] was coupled with the 1D core main plasma transport code ETS [4] including a core impurity transport code, developed within the framework of the ITM-TF. In this work a Fortran version of the ETS workflow was used, including the equilibrium code HELENA[12] and simple models for particle and energy sources as well as transport coefficients. ASDEX Upgrade Pulse No: 17151 equilibrium at 2.5s was imported into equilibrium and limiter CPOs, and the bounding surface separating the calculation domains between the core and edge codes calculated (at 95% of the normalized poloidal flux in the case below). These CPOs enter the HELENA code providing equilibrium to the core transport code and were used to create the SOLPS grid (Figure 15 left). The two codes were then called alternately and individually run until converged, with information about the boundary conditions transferred from one to the other, until convergence of the workflow is obtained.

For the most complicated test case, SOLPS treated all of the charge states of D, He, C, Ar and Ne (including the neutrals), a total of 42. The ETS treated D^+ and He^{+2} as main ions, and the core impurity code treated the individual charge states of C, Ar and Ne. The core codes did not, in this case, treat the neutrals. Electron and ion energy fluxes as well as D^+ and He^{+2} particle fluxes are passed from the core to the edge code. Values of density and ion temperature on the boundary are passed from SOLPS to the ETS and densities of C, Ar and Ne charge states to the core impurity code. SOLPS used a zero-flux boundary condition for neutrals, all of the charge states of C, Ar, Ne and for He^{+1} . Convergence was obtained with 5 iterations as it is shown in Figure 14. The results for the steady state electron temperature and density are shown in Figure 15; densities for C, Ne and Ar charge states in Figure 16.

Recently SOLPS has been modified so that it can be called to advance the edge plasma with changed boundary conditions. The coupling has thus been automatised as follows: the ETS Fortran workflow calls SOLPS just after the convergence loop, SOLPS receives as input the necessary boundary conditions from the core CPOs, runs for one or more time-steps and calculates new core CPOs with new boundary conditions based on the edge results, than the ETS continues with a new time-step.

4.2 TRANSPORT SIMULATIONS INCLUDING NTMS

A module which simulates the time behaviour of Neoclassical Tearing Modes (NTM) [40] can also be integrated in the ETS workflows. Here we present a proof-of-principle of the effect of NTMs on transport evolution in an ETS simulation. NTMs are resistive instabilities breaking the flux surfaces into magnetic islands at the rational surfaces $q = m/n$. The modes are destabilized by a loss of bootstrap current proportional to the plasma pressure. The simulated modes grow starting from a specified onset time, up to the saturated state. Their growth affects the local electron and ion temperature and density by changing the perpendicular transport coefficients around the mode location. The transport is modified by the NTM module, which adds a Gaussian perturbation of given amplitude and width to the unperturbed transport coefficients. This approach enables the reproduction of density and temperature profiles very close to the experimental ones.

Figure 18 presents the temporal evolution of the electron temperature and total perpendicular heat diffusivity profiles, during an ETS-NTM simulation performed for typical JET H-mode plasma conditions. The effect on these profiles of an $m/n = 2/1$ magnetic island, assumed to be located at $\rho_{\text{tor}} \sim 0.8$ is shown. The increase of radial transport due to the presence of this magnetic island leads to a flattening of the temperature profile around the 2/1 surface. The mode is predicted to grow up to a saturated island of 8 cm width on a resistive time scale of about 150 ms; this leads to a 16% drop in the stored energy.

4.3 FREE BOUNDARY EQUILIBRIUM COUPLED TO TRANSPORT

Coupling of a free-boundary equilibrium code to the ETS transport solver has recently been obtained in a version of the ETS workflow coupled to the CEDRES++ free boundary equilibrium code[41]. The CEDRES++ actor uses the same generic interfaces as used by fixed boundary codes within the ETS workflows, thus providing a full replacement for those. Figure 19 shows the result of the first test simulation of a vertical displacement event (VDE) for an ITER scenario. The simulation started from a static equilibrium at $t = 108.02\text{s}$. The VDE is forced by imposing a substantial voltage in two of the poloidal field coils (PFC1 and PFC6). As a result, the plasma moves downwards on a ~ 100 ms timescale, which is typical for ITER [42].

5. SYNTHETIC DIAGNOSTICS INTEGRATION

The ongoing efforts on synthetic diagnostic integration in the ITM-TF platform focus on reflectometry, neutron and NPA diagnostics and spectral MSE.

A full-wave 3D code (ERC3d) valid for both O and X-mode polarizations has been developed, ported and tested on the ITM platform and work is under way to enhance the kernel to cope with high levels of turbulence and high injection angles (Doppler reflectometry operation). A generic framework for neutron synthetic diagnostics has been integrated which is composed of three different modules: calculation of the effective solid angle of the detector from small plasma volumes (LINE21 code); a Directional Relativistic Spectrum Simulator (DRESS) to derive the energy

spectra and source rates of particles created in fusion reactions emitted in a specified direction and a diagnostic response function. Integration of JET neutron camera setup is ongoing. The integration of NPA diagnostics in the ITM platform was also carried out using modules of the ASCOT code package [43] and calculating the fraction of the tokamak chamber and born neutrals (with given pitch velocity) that are within the sight of the NPA collimator. A spectral MSE forward model [44] that calculates the emissivity for each MSE channel and the resultant radiance Balmer-alpha MSE spectra as well as the charge exchange of the plasma with the beam has been integrated. Full, half and third beam energy components are considered and a collisional-radiative beam-plasma model is used to determine the coupled densities of charged states along the diagnostic neutral beam path. Preliminary results on the MSE synthetic diagnostic validation on ASDEX Upgrade data (Pulse No: 26320) are presented in Figure 20, showing the simulated and experimental emissivities.

CONCLUSIONS

The EU ITM-TF standardized, modular and flexible integrated modelling framework allows building complex workflows for physics application and is a valuable environment to benchmark codes describing similar physics processes with different model sophistication, by interchanging those as modules within the same workflow. Besides, both the orchestration engine Kepler, and the ITM-TF developments performed in collaboration with the FP7 EUFORIA project [17] and the HLST[‡], allow to run workflows or only part of those (the main workflow residing on the central ITM Gateway cluster) on GRID or HPC-FF, thus rendering possible highly computationally demanding calculations.

The first application of the ITM-TF simulation chain coupling equilibrium reconstruction, refinement and linear MHD stability modules addressed edge stability of ASDEX Upgrade ELMy H-Mode and ITER hybrid scenario. Turbulence code interpretative runs starting from given experimental profiles of a JET hybrid discharge, challenging case near to stability threshold conditions, were performed with two different electromagnetic codes, a gyrofluid and a gyrokinetic one, within an ITM workflow. Only one radial position ($ra = 0.6$ in normalised radius) was found unstable in the gyrokinetic run, highlighting trapped-electron assisted ITG turbulence characteristics. A benchmark among EC beam/ray-tracing codes for a standard inductive H-mode ITER scenario for three different launching conditions, showed good agreement of the five EU codes even in the more demanding test cases, like central ECCD at high temperature, and beam focused close to the resonance region. Benchmarking of the European Transport Simulator (ETS) against ASTRA and CRONOS transport codes, on a JET discharge, showed very good agreement among the simulated quantities, laying the foundations for its usage for both predictive and interpretative runs on present devices and ITER.

Some selected examples of ITM scientific workflow applications have also been outlined. Automated direct coupling of a core and edge transport code was demonstrated for the particular case of steady state and multiple impurities. The effect of NTMs on heat transport coefficients and

[‡]<http://www.efda-hlst.eu/>

temperature profiles was reproduced via a dedicated NTM module incorporated in the ETS. Coupling of the ETS to a free boundary equilibrium solver was tested on a vertical displacement event (VDE) for an ITER scenario. Finally, ongoing efforts on the integration and testing of synthetic diagnostics in the ITM-TF platform have been reported, namely, the validation of spectral MSE forward model on ASDEX Upgrade data.

ACKNOWLEDGMENTS

This work, supported by the European Communities under the contract of Association between EURATOM and CEA, CCFE, ENEA, FOM, IPP, IPPLM, IST, Swiss Confederation, VR, was carried out within the framework of the Task Force on Integrated Tokamak Modelling of the European Fusion Development Agreement. Part of the research leading to these results received funding from the European Community's Research Infrastructures initiative of the 7th Framework Programme FP7 (2007-2013) under grant agreement No 211804 (EUFORIA). The views and opinions expressed herein do not necessarily reflect those of the European Commission.

REFERENCES

- [1]. Becoulet A, et al. 2007, *Computer Physics Communications* **177**(1-2):55 – 59.
- [2]. Strand P I, et al. 2010, *Fusion Engineering and Design* **85**(3-4):383 – 387.
- [3]. Imbeaux F, et al, 2010, *Computer Physics Communications* **181**(6): 987 – 998.
- [4]. Coster D, Basiuk V, Pereverzev G, Kalupin D, Zagórksi R, et al., 2010, *IEEE Transactions on Plasma Science* **38**, 2085.
- [5]. Konz C, et al, 2011, “First physics applications of the Integrated Tokamak Modelling (ITM-TF) tools to the MHD stability analysis of experimental data and ITER scenarios”, O2.103, 38th EPS Conference on Plasma Physics, Strasbourg. In *Europhysics Conference Abstracts Vol. 35G*, ISBN 2-914771-68-1.
- [6]. Figini L et al., 2012, *EPJ Web of Conferences* 32, 01011.
- [7]. Kalupin D, et al., 2011, “Verification and Validation of the European Transport Solver”, P4.111, 38th EPS Conference on Plasma Physics, Strasbourg. In *Europhysics Conference Abstracts Vol. 35G*, ISBN 2-914771-68-1.
- [8]. Coster D P , Klingshirn H-J, et al., 2012, “Core-Edge Coupling: developments within the EFDA Task Force on Integrated Tokamak Modelling”, P1.073, 39th EPS Conference on Plasma Physics& 16th Int. Congress on Plasma Physics, Stockholm.
- [9]. Coelho R, et al., 2013, *Fusion Science and Technology* **63**(1), 1-8..
- [10]. Zwingmann W, 2003, *NuclEAR Fusion* **43**, 842.
- [11]. Zwingmann W, et al., 2008, *PLASMA 2007*, AIP Conf. Proc. Vol. **993**, 11.
- [12]. Huysmans G, Goedbloed J, and Kerner W, 1991, in *CP90 Conf. on Comp. Physics Proc*, page 371, World Scientific Publ. Co.
- [13]. Luetjens H, Bondeson A, Sauter O, 1996, *Computer Physics Communications* **97**, 219

- [14]. Huysmans G T A, et al., 2001, *Physics of Plasmas* **8**(10), 4292.
- [15]. Liu Y Q, Bondeson A, Fransson C M, Lennartson B, and Breitholtz C, 2000, *Physics of Plasmas* **7**, 3681.
- [16]. Zwingmann W, et al, 2010, “Validation Procedure of the Tokamak Equilibrium Reconstruction Code EQUAL with a Scientific Workflow System”, P4-180, 37th EPS Conference on Plasma Physics, Dublin.
- [17]. Coster D P, Strand P, Contributors to the EUFORIA Project, 2010, “EUFORIA: Exploring E-Science for Fusion”, in *Advances in Parallel Computing*, 19, 520 – 529; DOI 10.3233/978-1-60750-530-3-520
- [18]. Scott B, 2005, *Physics of Plasmas* **12**, 102307.
- [19]. Scott B, 2010, *Physics of Plasmas* **17**, 102306
- [20]. Scott B, 2000, *Physics of Plasmas* **7**, 1845--1856.
- [21]. Scott B, 2001, *Physics of Plasmas* **8**, 447--458.
- [22]. Scott B, 2003, *Plasma Physics and Controlled Fusion* **45**, A385--A398.
- [23]. Naulin V, 2003, *Physics of Plasmas* **10** (10) , 4016--4028.
- [24]. Scott B, 2006, *Plasma Physics and Controlled Fusion* **48**, B277-B293
- [25]. Scott B, 2005, *Physics of Plasmas* **12**(6), 062314.
- [26]. Scott B, 1997, *Plasma Physics and Controlled Fusion* **39**, 1635-1668.
- [27]. Kalupin D et al., 2012, “The European Transport Solver: an integrated approach for transport simulations in the plasma core”. 4-TH P2-01, Proc. 24th IAEA Fusion Energy Conference 2012, San Diego, US.
- [28]. Basiuk V, Huynh Ph, et al., 2010, “European Transport Solver: first results, validation and benchmark”, P 1.1009, 37th EPS Conference on Plasma Physics, Dublin;
- [29]. Peysson Y, et al, 2012, *Plasma Physics and Controlled Fusion* **54**, 045003.
- [30]. Farina D, 2007, *Fusion Science and Technology* **52**, 154.
- [31]. Westerhof E, Implementation of TORAY at JET (Rijnhuizen Report, 1989) RR-89-183.
- [32]. Poli E, et al, 2001, *Computer Physics Communications* **136**, 90.
- [33]. Marushchenko N B, et al, 2007, *Journal of Plasma and Fusion Research* **2**, S1000.
- [34]. Figini L et al., in preparation.
- [35]. Pereverzev G and Yushmanov P N, 2002, “ASTRA Automated System for Transport Analysis in a Tokamak”, Max-Planck Institut fur Plasmaphysik, IPP 5/98.
- [36]. Artaud J-F, Basiuk V, Imbeaux F et al., 2010, *Nuclear Fusion* **50**, 043001.
- [37]. Coster D P, 2009, *Journal of Nuclear Materials* **390–391**, 826.
- [38]. Schneider R, et al., 2006, *Contribution to Plasma Physics* **46**, 3, DOI 10.1002/ctpp.200610001.
- [39]. Äkäslompolo S, et al., 2012, “Preparing tokamak 3D wall and magnetic data for particle tracing simulations”, P5.058, 39th European Physical Society Conference on Plasma Physics, Stockholm.
- [40]. Sauter O, et al. 2002 *Plasma Physics and Controlled Fusion* **44** 1999

- [41]. Hertout P, et al, 2011, Proceedings of Symposium of Fusion Technology 2010, Fusion Engineering and Design, vol. **86**, pp. 1045-1048
- [42]. Gribov T, et al., 2007, Nuclear Fusion **47**, S385–S403.
- [43]. Heikkinen J A, Sipilä S K, et al., 1993, Computer Physics Communications **76** (2), 215.
- [44]. Dinklage A, Reimer R, et al., 2011, Fusion Science Technology **59**, 406.

APPENDIX: LIST OF ITM-TF CONTRIBUTORS

M. Airila¹, S. Äkäslompolo², L. Allegretti³, L. Alves⁴, T. Aniel³, L. Appel⁵, J-F. Artaud³, O. Asunta², C-V. Atanasiu⁶, F. Aumayr⁷, O. Barana³, M. Baruzzo⁸, V. Basiuk³, R. Bilato⁹, J. Bizarro⁴, E. Blanco²¹, J. Blum¹⁰, T. Bolzonella⁸, X. Bonnin¹¹, D. Borodin¹², A. Bottino⁹, C. Boulbe¹⁰, S. Brémond³, S. Briguglio¹³, Y. Buravand³, A. Cardinali¹³, C. Cianfarani¹³, J. Citrin¹⁴, R. Coelho⁴, D. Coster⁹, G. Csepány¹⁷, D. Dimopoulos¹⁸, A. Dinklage¹⁹, C. DiTroia¹³, C. Dritselis¹⁸, D. Dumitru⁶, R. Dumont³, E. Fable⁹, G L Falchetto³, D. Farina²⁰, B. Faugeras¹⁰, J. Ferreira⁴, L. Figini²⁰, A. Figueiredo⁴, G. Fogaccia¹³, V. Fusco¹³, K. Gal⁴¹, J. Garcia³, P. Garcia-Muller²¹, L. Garzotti⁵, J. Geiger⁹, E. Giovannozzi¹³, G. Giruzzi³, V. Goloborodko¹⁶, R. Goswami³, B. Guillerminet³, S. Hacquin³, A. Hannan²², J. Heikkinen¹, T. Hellsten²², S. Heuraux²³, J. Hillairet³, E. Hirvijoki², J. Hobirk⁹, D. Hogewey¹⁴, L. Höök²², P. Huynh³, K. Igenbergs²⁴, F. Imbeaux³, H. Isliker¹⁵, I. Ivanova-Stanik²⁵, S. Janhunen², F. Jenko⁹, T. Johnson²², S. Kakarantzas¹⁸, N. Kanaris²⁶, S. Kassinos²⁶, A. Keim⁷, V. Kiptily⁵, A. Kirschner¹², T. Kiviniemi², H-J. Klingshirn⁹, F. Köchl⁷, Y. Kominis³⁵, T. Korpilo², L. Kos²⁷, T. Koskela², S. Kulovec²⁷, C. Lechte²⁸, E. Lerche²⁹, X. Litaudon³, F. Liu³, Y. Liu⁵, J. Lönnroth⁵, T. Lunt⁹, G. Manduchi⁸, N. Marushchenko¹⁹, S. Mastrostefano³⁰, R. Mayo²¹, J. Miettunen², S. Moradi³¹, D. Moreau³, P. Moreau³, A. Morillas²¹, D. Muir⁵, Q. Mukhtar²², F. Nabais⁴, E. Nardon³, F. Nave⁴, A.H. Nielsen³², R. Nouailletas³, S. Nowak²⁰, M. O'Mullane⁵, M. Ottaviani³, M. Owsiak³³, V. Pais⁶, B. Palak³³, A. Papadopoulos³⁵, G. Papp¹⁷, N. Pelekasis¹⁸, Y. Peysson³, T. Pisokas¹⁵, M. Plociennik³³, G. Pokol¹⁷, E. Poli⁹, G. Poulipoulis³⁶, I. Pusztai³¹, H. Radhakrishnan²⁶, N. Ravenel³, H. Reimerdes³⁷, D. Reiser¹², M. Romanelli⁵, J. Rydén³¹, A. Salmi¹, T. Samaras³⁵, O. Sauter³⁶, P. Scheier³⁷, K. Schmid⁹, M. Schneider³, K. Schöpf¹⁶, B. D. Scott⁹, J. Signoret³, F. Silva⁴, S. Sipilä², P. Siren¹, A. Sirinelli⁵, A. Snicker², R. Stankiewicz²⁵, J. Storrs⁵, P. Strand³⁸, E. Sundén³⁹, T. Tala¹, S. Tholerus²², G. Throumoulopoulos³⁶, K. Tokesi⁴⁰, C. Tsironis³⁵, D. Tskhakaya¹⁶, O. Tudisco¹³, J. Urban³, D. V.Eester²⁹, L. Villard³⁶, F. Villone³⁰, B. Viola¹³, S. Viorica⁶, G. Vlad¹³, I. Voitsekhovitch⁵, E. Westerhof¹⁴, R. Wieggers¹⁴, M. Wischmeier⁹, D. Yadykin³⁸, P. Zestanakis³⁵, T. Zok³³

1. VTT Technical Research Centre of Finland, Association Euratom-TEKES, P O Box 1000, 02037 VTT, Finland
2. Department of Applied Physics, Aalto University, Association Euratom-TEKES, PO Box 13500, FI-00076 AALTO, Finland

3. CEA, IRFM, F-13108 Saint-Paul-lez-Durance, France
4. Associação EURATOM/IST, Instituto de Plasmas e Fusão Nuclear, Instituto Superior Técnico, Universidade Técnica de Lisboa 1049-001 Lisboa, Portugal
5. EURATOM/CCFE Fusion Association, Culham Science Centre, Abingdon OX14 3DB UK
6. National Institute for Laser, Plasma and Radiation Physics, Association MEDC-EURATOM, Bucharest, Romania
7. Association EURATOM-ÖAW/ATI, Atominstitut, TU Wien, 1020 Vienna, Austria
8. Associazione EURATOM-ENEA sulla Fusione, Consorzio RFX, 29127 Padova, Italy
9. Max-Planck-Institut für Plasmaphysik, EURATOM-IPP Association, Garching, Germany
10. Univ. Nice Sophia Antipolis, Lab. JA Dieudonne, UMR 7351, F-06108 Nice 02, France
11. CNRS-LIMHP, Université Paris XIII, F-93430 Villetaneuse, France
12. Institut für Energie und Klimaforschung Plasmaphysik, Forschungszentrum Jülich, Association Euratom-FZJ, Germany
13. Associazione Euratom-ENEA sulla Fusione, C.R. ENEA-Frascati, Via E. Fermi 45, 00037 Frascati, Roma, Italy
14. FOM Institute DIFFER, Association EURATOM-FOM, Nieuwegein, Netherlands
15. Section of Astrophysics, Astronomy and Mechanics, Department of Physics, University of Thessaloniki, Association Euratom-Hellenic Republic, Thessaloniki, Greece
16. Association EURATOM-ÖAW, Institute for Theoretical Physics, University of Innsbruck, A-6020, Innsbruck, Austria
17. Department of Nuclear Techniques, Budapest University of Technology and Economics, Association EURATOM, H-1111 Budapest, Hungary
18. Department of Mechanical Engineering, University of Thessaly, Pedion Areos, Volos 38334, Greece - Association Euratom-Hellenic Republic
19. Max Planck Institut für Plasmaphysik, EURATOM Association, Greifswald, Germany
20. Istituto di Fisica del Plasma CNR, Euratom-ENEA-CNR Association for Fusion, Milan, Italy
21. Asociación EURATOM CIEMAT, Madrid 28034, Spain
22. Association EURATOM-VR, Fusion Plasma Physics, EES, KTH, SE-10037 Stockholm, Sweden
23. Université de Lorraine, IJL, UMR 7198, BP 70233, Vandoeuvre , F-54506 Cedex, France
24. Vienna Univ. Technol., Inst. Appl. Phys., A-1034 Vienna, Austria
25. Institute of Plasma Physics and Laser Microfusion, EURATOM Association, 00-908 Warsaw, Poland
26. Computational Sciences Laboratory – UCY-CompSci, Department of Mechanical and Manufacturing Engineering, University of Cyprus, Nicosia, Cyprus
27. University of Ljubljana, Faculty of Mech. Eng., Askerceva 6, SI-1000 Ljubljana, Slovenia
28. Institute for Plasma Research, University of Stuttgart, 70569 Stuttgart, Germany
29. Ecole Royale Militaire - Koninklijke Militaire School, Laboratoire de Physique des Plasmas, B - 1000 Brussels, Belgium

30. Associazione EURATOM/ENEA/CREATE, DIEI, Università degli Studi di Cassino e del Lazio Meridionale, Via Di Biasio 43, 03043 Cassino (FR), Italy
31. Nuclear Engineering, Department of Applied Physics, Chalmers University of Technology, Euratom-VR Association, SE-35296 Göteborg, Sweden
32. Association EURATOM-DTU, 3400 Roskilde, Denmark
33. Poznan Supercomputing and Networking Center (PSNC), IChB PAS, Noskowskiego 12/14, Poznan, Poland
34. School of Electrical and Computer Engineering, National Technical University of Athens, Association EURATOM-Hellenic Republic, Zografou, Athens 15773, Greece
35. University of Ioannina, Association Euratom – Hellenic Republic, Section of Theoretical Physics, Ioannina, Greece
36. Ecole Polytechnique Federale de Lausanne (EPFL), Centre de Recherches en Physique des Plasmas (CRPP), Association Euratom-Confederation Suisse, Lausanne, Switzerland
37. Institut für Ionenphysik und Angewandte Physik, Universität Innsbruck
38. Department of Earth and Space Sciences, Chalmers University of Technology, Euratom-VR Association, SE-352 96 Göteborg, Sweden
39. Uppsala University, VR-Euratom Association, Box 516, 751 20 Uppsala, Sweden
40. Institute of Nuclear Research of the Hungarian Academy of Sciences (ATOMKI), 3401 Debrecen, Hungary
41. Institute for Particle and Nuclear Physics, Wigner Research Centre for Physics, Hungarian Academy of Sciences, EURATOM Association HAS, POB 49, H-1525, Budapest, Hungary

Case	R_m (m)	z_m (m)	α (°)	β (°)	w_0 (m)	d (m)
EL25	9.27	0.62	0	25	0.030	0.00
EL40	9.27	0.62	0	40	0.030	0.00
UL	6.90	4.18	48	18	0.021	1.62

Table I: Launching conditions used in the benchmark. The poloidal and toroidal launching angles are defined as $\alpha = \tan^{-1}(k_{0,z}/k_{0,R})$ and $\beta = \sin^{-1}(k_{0,\phi}/k_0)$, where $(k_{0,R}, k_{0,\phi}, k_{0,z})$ are the cylindrical wave vector components of the launched wave. The beam has a Gaussian profile, with waist w_0 at a distance d from the launching point.

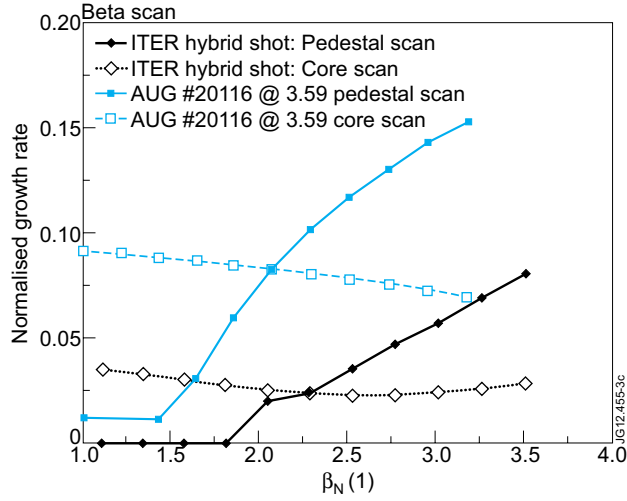


Figure 3: Core and pedestal scans of the normalized plasma beta for ASDEX Upgrade type-I ELM My Pulse No: 20116 (blue) and an ITER hybrid scenario (black) [9]. The dashed lines show modification of the plasma β_N via modification of the core pressure profile while keeping the pedestal pressure unchanged. The solid lines, on the other hand, show modification of the plasma β_N via scaling of the entire pressure profile.

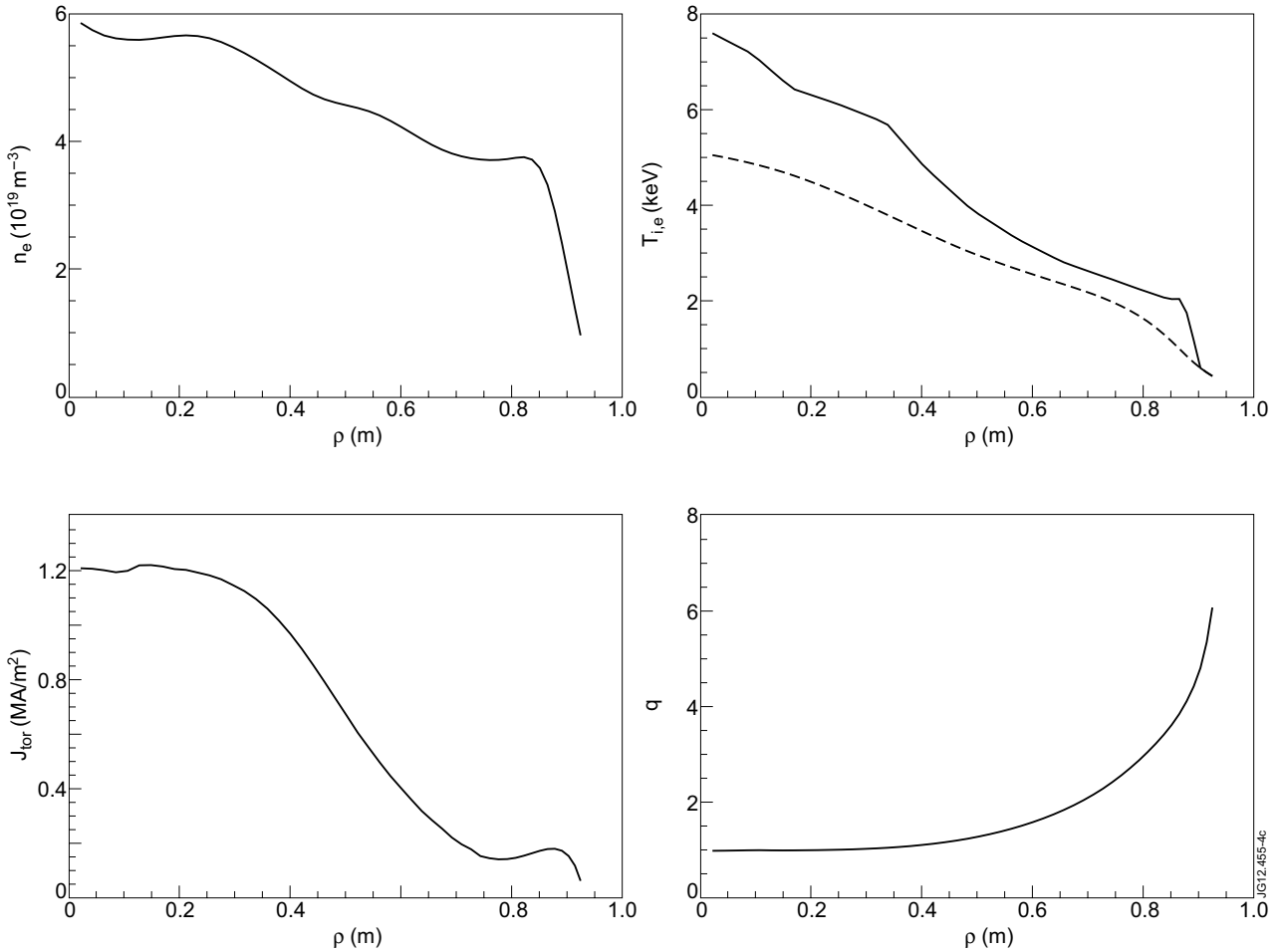


Figure 4: Profiles of the electron density, electron (dashed) and ion temperatures (full line), toroidal current and pitch parameter q , for the JET Pulse No: 77922 at 7.7 seconds given by the TRANSP interpretation through coreprof and equilibrium CPOs in the database case as discussed in the text.

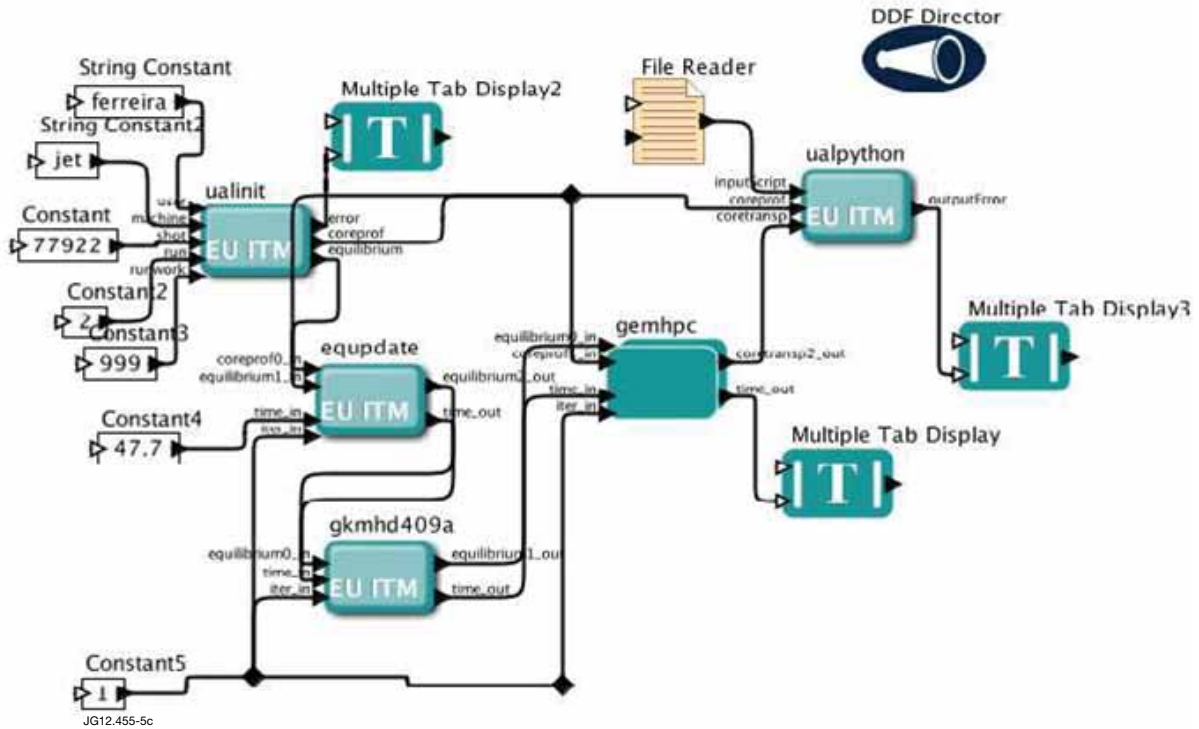


Figure 5: Turbulence workflow: JET shot data are read from the ITM database, the actor EQUIPDATE provides equilibrium profile data and the equilibrium boundary, ie the separatrix to actor GKMHD which adds the metrics information; both equilibrium_CPO and coreprof_CPO are input to the turbulence actor GEMHPC which runs in batch GEM gyrofluid flux-tube code in parallel on the HPC-FF.

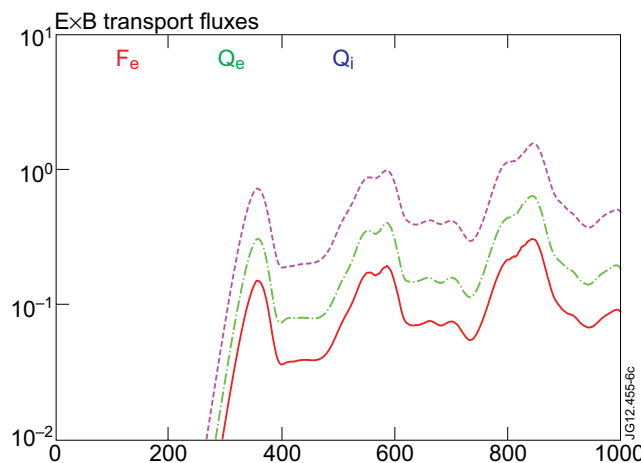


Figure 6: Time traces of the electron particle (F_e) and electron and ion conductive heat fluxes (Q_e/Q_i), showing very strong bursts on a logarithmic scale. The run needs to go to perhaps 2000 τ_{GB} for full saturation, but this is sufficient to display the mode structure of the turbulence. The initial density blob is at nonlinear amplitude but covers a small fraction of the spatial domain; hence the small initial amplitude and the appearance of a linear growth phase.

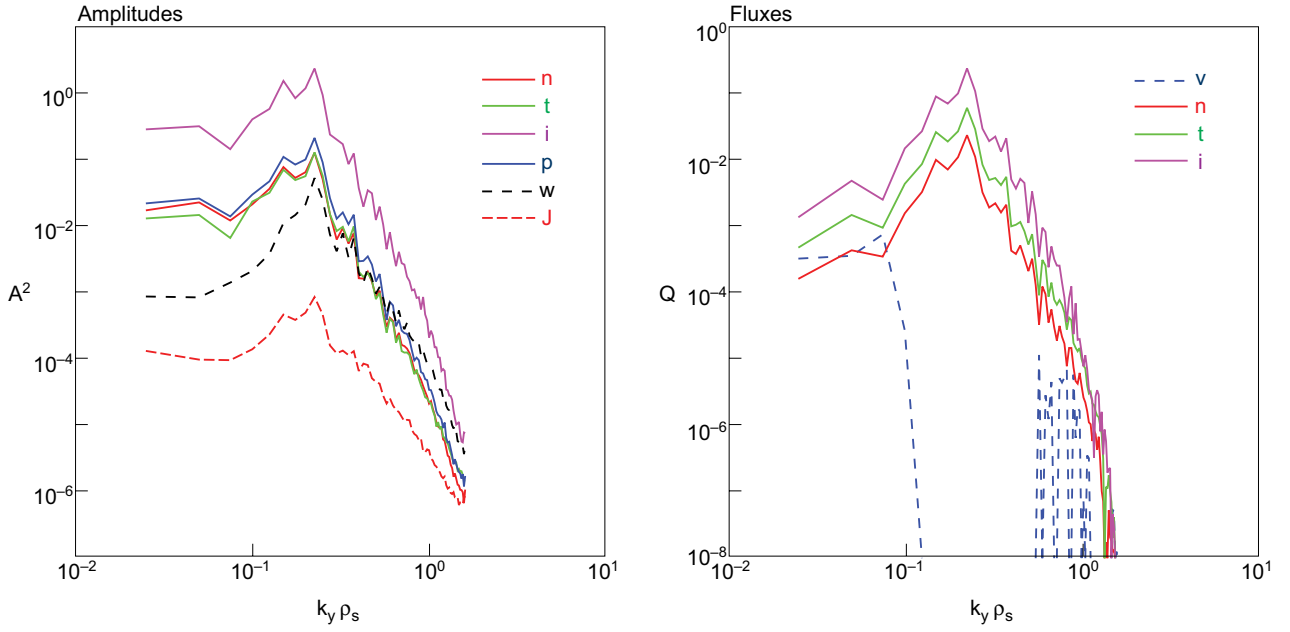


Figure 7: Spectra of the squared amplitudes (left) and transport fluxes (right) of various quantities, for a snapshot at the end of the delta-FEFI run. (left), the curves n , t , i , p , w , j , refer to the fluctuation power spectra of n_e , T_e , T_i , ϕ , vorticity, and current, respectively; (right) the curves v , n , t , i , refer to the magnetic flutter electron heat flux and the $E \times B$ fluxes of particles and electron and ion heat, respectively. All spectra peak in the same range except that the magnetic flutter is negative in the energy-producing range (ie, this is not a case driven by magnetic fluctuations, but the electromagnetic character is due to the effect of the inductive electric field in the parallel responses). The ion temperature fluctuations amplitudes and the ion heat flux are the largest.

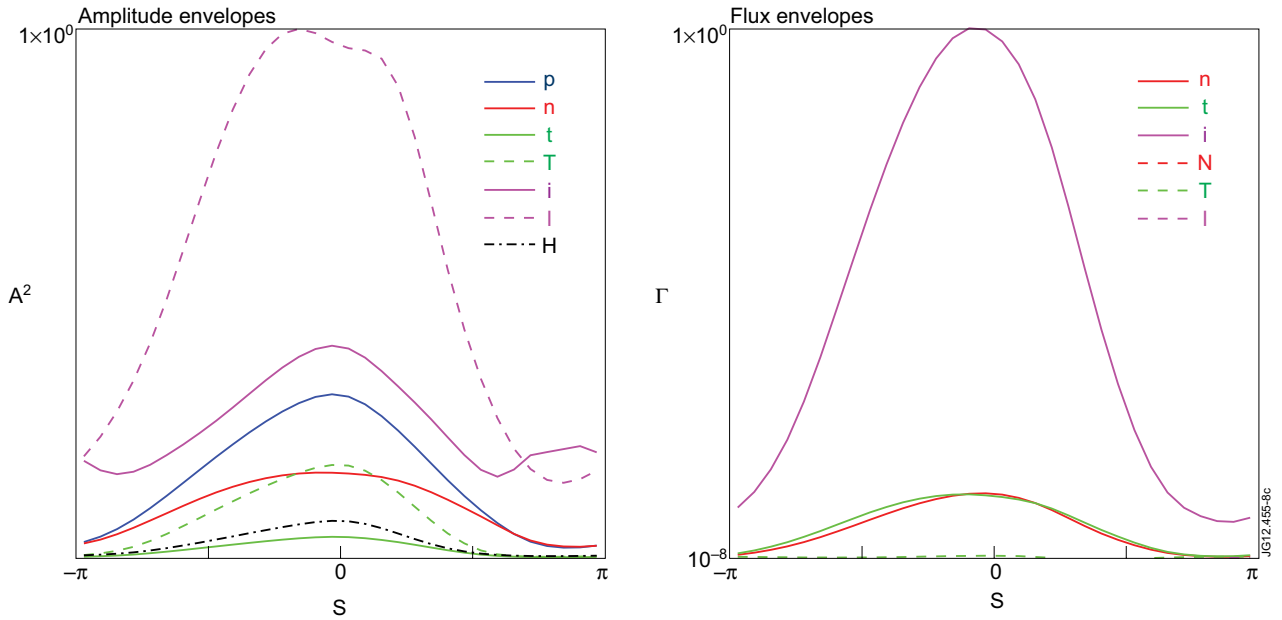


Figure 8: Parallel envelope structure of the squared amplitudes (left) and transport fluxes (right) of various quantities, for a snapshot at the end of the delta-FEFI run. (left) the curves p , n , t/T , i/I , H refer to Φ , n_e , T_e , T_i , and h_e respectively, where h_e is the nonadiabatic part of n_e . (right) the curves n , t , i refer to the $E \times B$ fluxes of particles and electron and ion heat, respectively, and N , T , I refer to the magnetic flutter fluxes of the same transport channels. For the temperatures, capital/lower-case letters refer to the perpendicular/parallel energy components. The perpendicular ion temperature is the largest and most strongly ballooned fluctuation, and the ion heat flux is the largest, all in relative units. The magnetic flutter channels are very small. This is indicative of ITG energetics.

Figure 9: Spatial morphology of electron density fluctuations in the perpendicular plane, at a snapshot just after the largest peak in the transport fluxes ($t = 860$). This shows the "streamer break" as positive and negative perturbations in the streamer chain move to the outside/inside (down-/up-gradient) respectively, a signature of the convective $E \times B / \Delta \cdot f$ nonlinearity. In the gyrofluid case the degree of small-scale radial hash on the structures is more visible, since every degree of freedom is subject to field line connection, while here in the gyrokinetic case the large influence of trapped electrons in the overall dynamics produces much smoother contour structure.

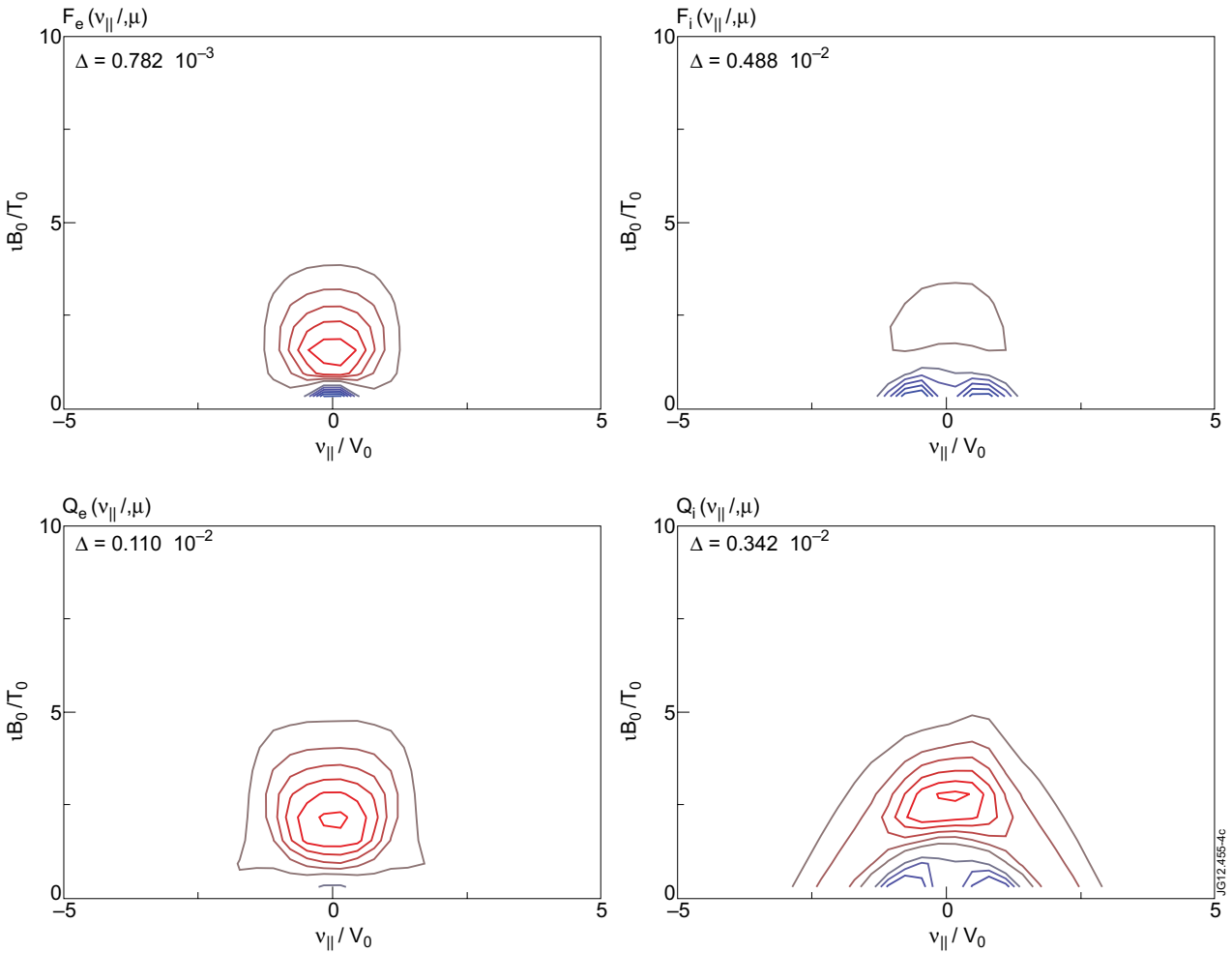
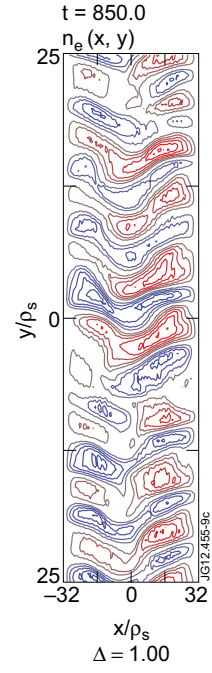


Figure 10: Velocity-space distribution of the $E \times B$ particle and heat fluxes in the electrons and ions, in a snapshot at the end of the run. The trapped zone is roughly the 60-degree cone centered upon the vertical axis where $v_{\parallel} = 0$. Almost all of the activity in the ions, and essentially all of it in the electrons, is in the trapped zone. These trapped-electron features together with the dominant ITG energetics yield the description "trapped-electron enhanced ITG turbulence".

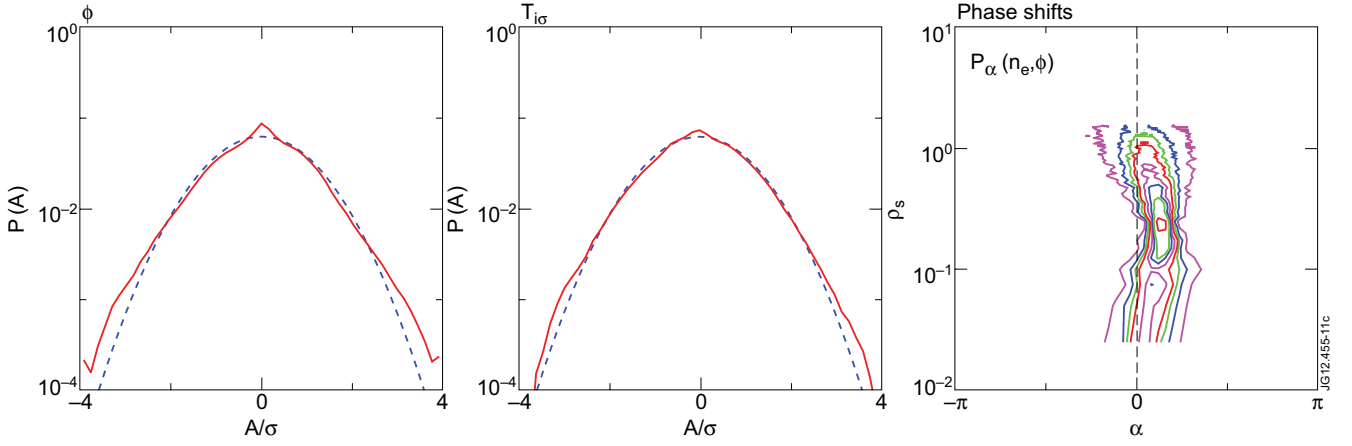


Figure 11: Amplitude PDF of electrostatic potential (left) and ion temperature fluctuations (centre) and phase shift distributions of n_e relative to Φ (right), for the time interval $400 < t/\tau_{GB} < 1000$ covering three of the bursts. These PDFs (red curves) are close to Gaussian (dashed curves), while those of the vorticity and current (not shown) are flatter. The phase shifts (right) are positive but closer to zero than to $\pi/2$. In these terms the physics is still turbulence as these signals are very common to any member of the drift wave turbulence class. The correlation lengths over the same interval (not shown) are $\lambda_x = 7.97 \rho_s$ and $\lambda_y = 5.46 \rho_s$, reflecting influence of the streamers as $\lambda_y > \lambda_x$ is common otherwise.

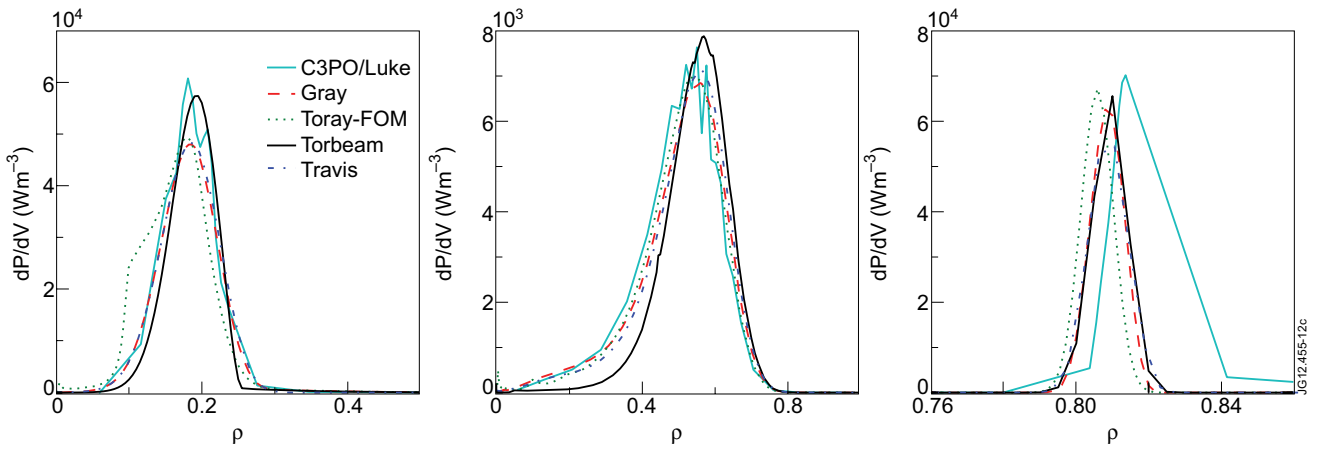


Figure 12: Power density profiles computed for the launching conditions of Table 1: EL25 (left), EL40 (center) and UL (right).

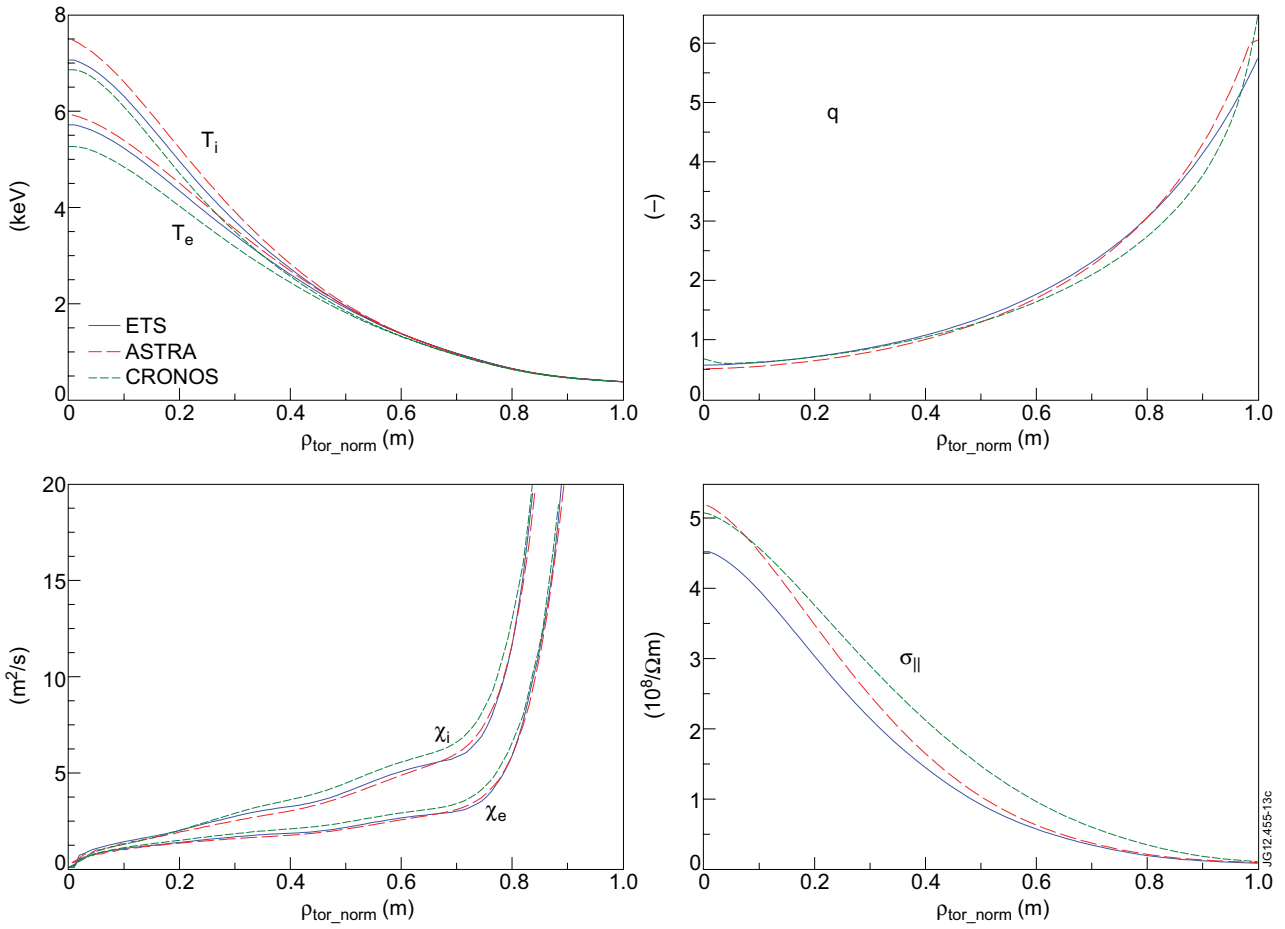


Figure 13: Benchmarking between ETS (blue), ASTRA (red) and CRONOS (green) integrated modelling transport codes for the conditions of JET hybrid Pulse No: 77922.

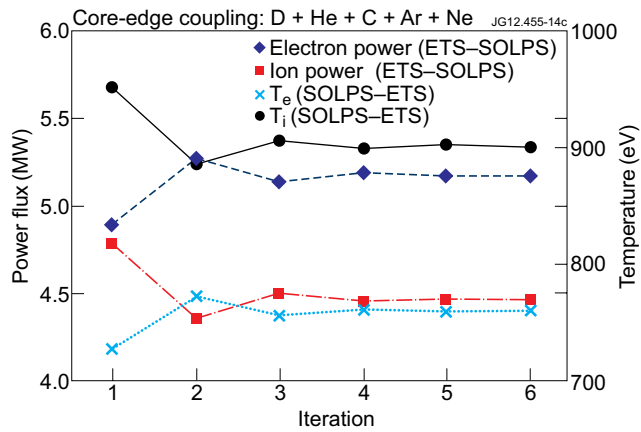


Figure 14: Core-edge workflow convergence of the boundary powers and temperatures with respect to iteration number.

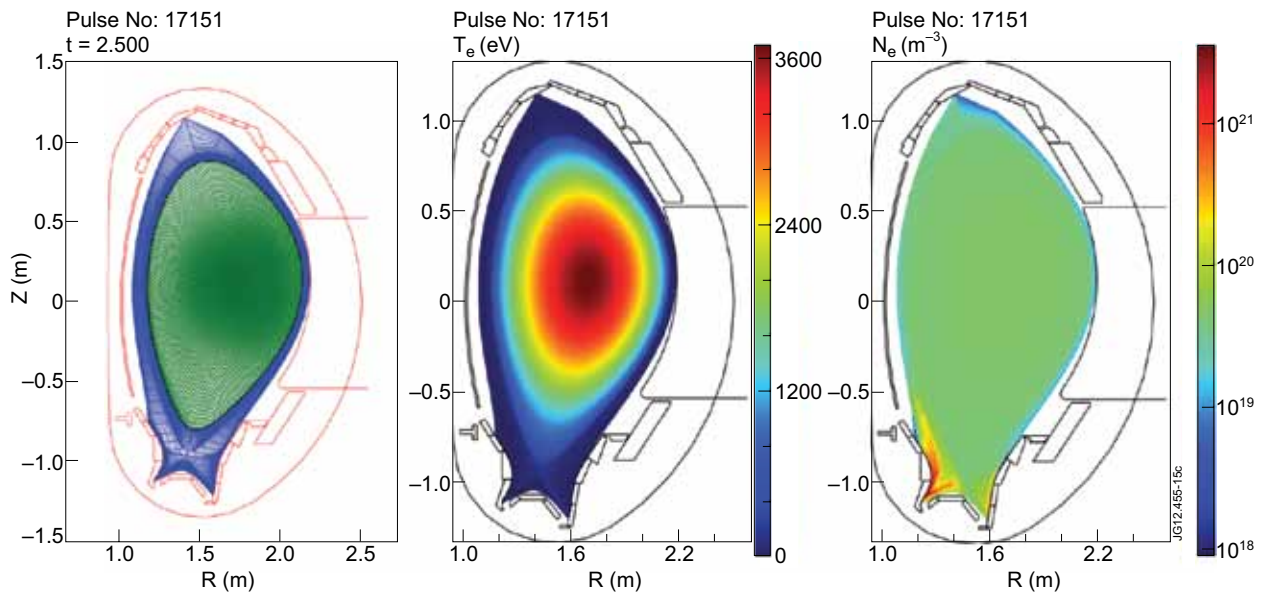


Figure 15: Left, the combined core and edge grids for ASDEX Upgrade Pulse No: 17151. All plot data are derived from ITM CPOs. T_e (center) and n_e (right) for the final state of the D+He+C+Ar+Ne case.[8]

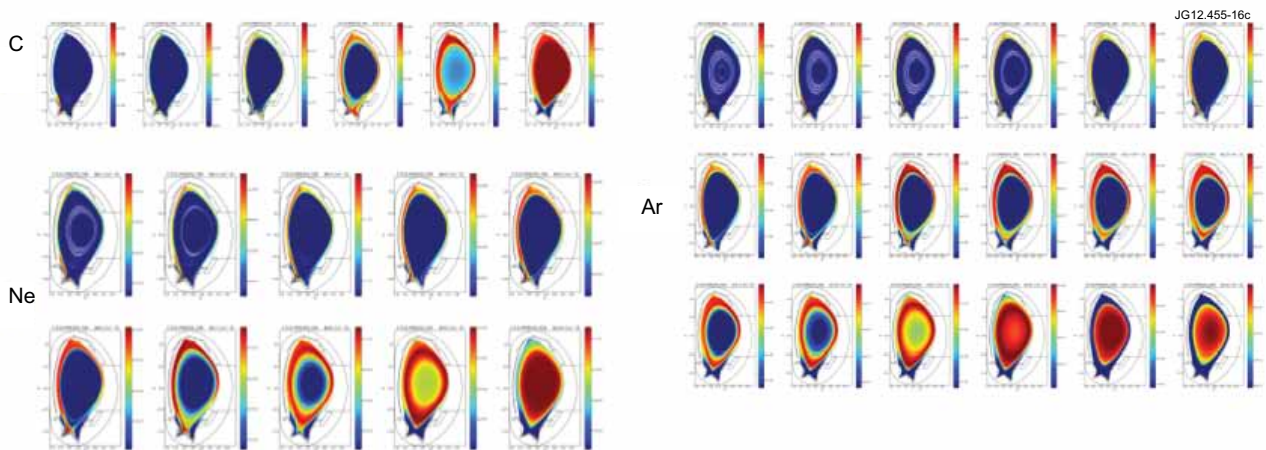


Figure 16: Density plots in the steady state for all the charges states of C Ne (left, top bottom) and Ar (right)[8].

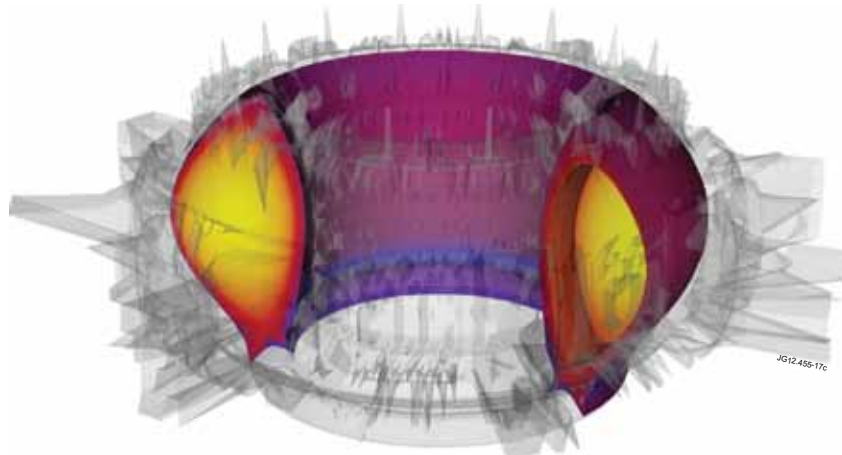


Figure 17: Visualization of the core-edge coupled simulation results: T_e calculated in the core with the ETS, in the edge with SOLPS, within the 3D deformed first wall of ASDEX Upgrade obtained using a ray-tracing rasterization and smoothing [39]. All data is stored in CPOs and plot with VisIT.

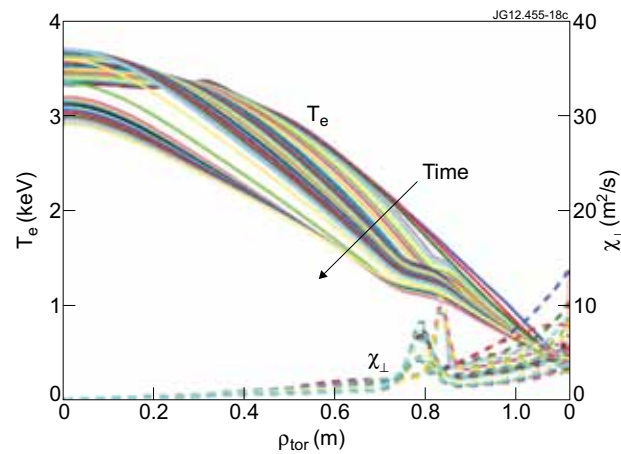


Figure 18: Modification of the heat transport coefficient by NTMs, assumed to be located at $\rho_{tor} \sim 0.8$, and its effect on the electron temperature profile.

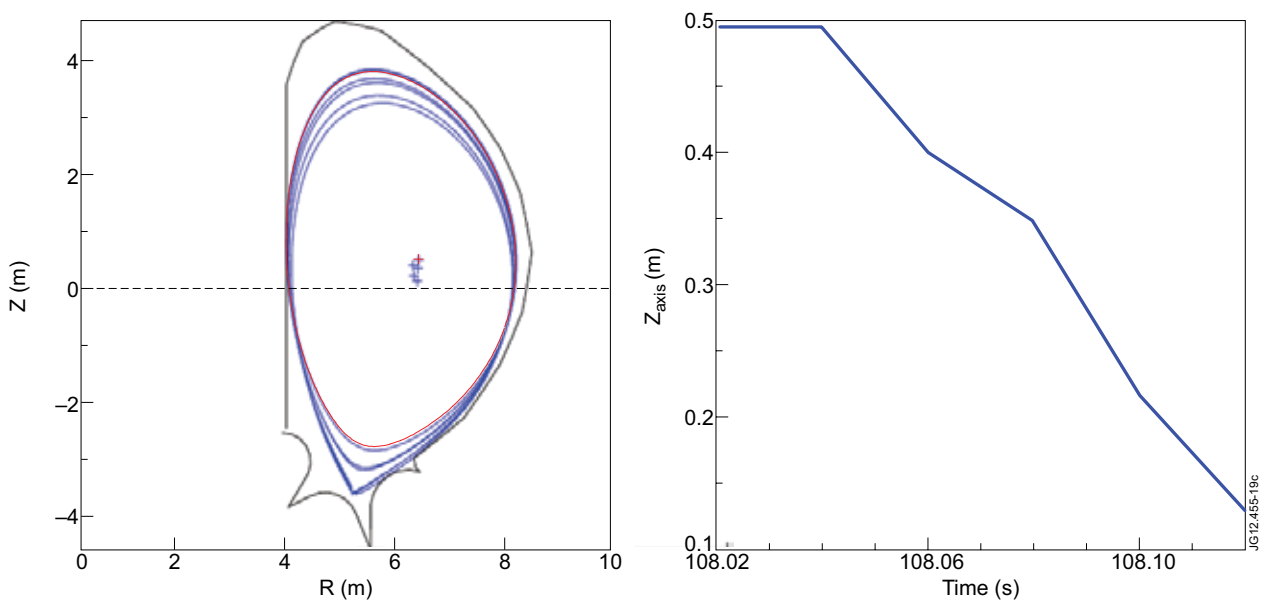


Figure 19: Imposed VDE (left, time evolution of the last closed magnetic flux surface; right, time evolution of the magnetic axis height).

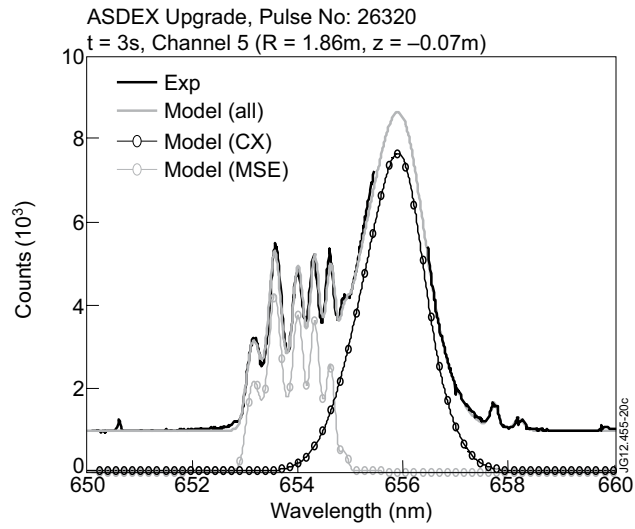


Figure 20: MSE emissivity wavelength spectra for ASDEX Upgrade Pulse No: 26320. The contribution from half and third beam energy components, beam divergence and unshifted D_α emission are shown. An offset of ~ 1000 counts is added to the MSE+CX synthetic counts to account for the characteristic background level of the measured signal by the CCD.